PET Imaging Using ^{89}Zr-Labeled StarPEG Nanocarriers Reveals Heterogeneous Enhanced Permeability and Retention in Prostate Cancer

Niranjan Meher[1,2], Anil P. Bidkar[1], Anju Wadhwa[1], Kondapa Naidu Bobba[1], Suchi Dhrona[1], Chandrashekhar Dasari[1,6], Changhua Mu[1], Cyril O.Y. Fong[1], Juan A. Cámara[4], Umama Ali[1], Megha Basak[1], David Bulkley[8], Veronica Steri[4], Shaun D. Fontaine[3], Jun Zhu[7], Adam Oskowitz[6], Rahul R. Aggarwal[4], Renuka Sriram[1], Jonathan Chou[7], David M. Wilson[1,4], Youngho Seo[1,4], Daniel V. Santi[3], Gary W. Ashley[3], Henry F. VanBrocklin[1,4], and Robert R. Flavell[1,4,5]

ABSTRACT

The enhanced permeability and retention (EPR) effect controls passive nanodrug uptake in tumors and may provide a high tumor payload with prolonged retention for cancer treatment. However, EPR-mediated tumor uptake and distribution vary by cancer phenotype. Thus, we hypothesized that a companion PET imaging surrogate may benefit EPR-mediated therapeutic drug delivery. We developed two ^{89}Zr-radiolabeled nanocarriers based on 4-armed starPEG$_{40kDa}$ with or without talazoparib (TLZ), a potent PARP inhibitor, as surrogates for the PEG-TLZ$_4$ therapeutic scaffold. For PET imaging, PEG-DFB$_4$ and PEG-DFB$_1$-TLZ$_3$ were radiolabeled with ^{89}Zr by replacing one or all four copis of TLZ on PEG-TLZ$_4$ with deferoxamine B (DFB). The radiolabeled nanodrugs [^{89}Zr]PEG-DFB$_4$ and [^{89}Zr]PEG-DFB$_1$-TLZ$_3$ were tested *in vivo* in prostate cancer subcutaneous (s.c.) xenografts (22Rv1, LTL-545, and LTL-610) and 22Rv1 metastatic models. Their EPR-mediated tumoral uptake and penetration was compared with CT26, a known EPR-high cell line. MicroPET/CT images, organ biodistribution, and calculated kinetic parameters showed high uptake in CT26 and LTL-545 and moderate to low uptake in LTL-610 and 22Rv1. MicroPET/CT and high-resolution autoradiographic images showed nanocarrier penetration into highly permeable CT26, but heterogeneous peripheral accumulation was observed in LTL-545, LTL-610, and 22Rv1 s.c. xenografts and metastatic tumors. CD31 staining of tumor sections showed homogenous vascular development in CT26 tumors and heterogeneity in other xenografts. Both [^{89}Zr]PEG-DFB$_4$ and [^{89}Zr]PEG-DFB$_1$-TLZ$_3$ showed similar accumulation and distribution in s.c. and metastatic tumor models. Both nanocarriers can measure tumor model passive uptake heterogeneity. Although heterogeneous, prostate cancer xenografts had low EPR. These starPEG nanocarriers could be used as PET imaging surrogates to predict drug delivery and efficacy.

Introduction

Prostate cancer remains a major global health challenge with the second highest cause of cancer death in men, with an unmet clinical need for improved therapeutic options (1, 2). Nanocarriers have emerged as a promising approach for delivering drugs to the tumor site, leveraging the enhanced permeability and retention (EPR) effect to increase tumoral accumulation (3–6). The EPR effect refers to the increased permeability and retention of macromolecules in the tumor microenvironment, which is characterized by leaky blood vessels and impaired lymphatic drainage (7–9). This effect has been demonstrated in a variety of solid tumors and is thought to be a key mechanism by which nanocarriers can accumulate selectively at the site of the tumor for a long period of time.

However, multiple factors, including tumor vasculature and macrophages, have been shown to play a critical role in regulating the EPR-mediated selective accumulation and distribution of nanocarriers in tumors (7, 9–12). Tumor blood vessels are highly heterogeneous and can vary significantly in terms of size, shape, and permeability (13, 14). Macrophages, which are present in high numbers in the tumor microenvironment, can also play a role in the uptake and distribution of nanocarriers (10). In particular, solid tumors with poor vasculature may not allow nanocarriers to penetrate deep into the tumor tissue, potentially influencing therapeutic efficacy (15). For instance, nontargeted polymer nanostars demonstrated efficient tumor penetration and accumulation in highly vascular CT26 tumors but were unable to penetrate deep into BxPC3 tumors with low vascularity (15). Prior reports demonstrated low peripheral tumor accumulation of nontargeted nanocarriers in multiple prostate cancer models like CWR22Rv1, DU145, and PC3, highlighting their EPR-low status (15–17). Previously, we developed

---

[1]Department of Radiology and Biomedical Imaging, University of California San Francisco, San Francisco, California. [2]National Institute of Pharmaceutical Education and Research, Lucknow, India. [3]ProLynx Inc., San Francisco, California. [4]Helen Diller Family Comprehensive Cancer Center, University of California San Francisco, San Francisco, California. [5]Department of Pharmaceutical Chemistry, University of California San Francisco, San Francisco, California. [6]Division of Vascular and Endovascular Surgery, University of California San Francisco, San Francisco, California. [7]Department of Medicine, University of California San Francisco, San Francisco, California. [8]Department of Biochemistry and Biophysics, University of California San Francisco, San Francisco, California.

Corresponding Author: Robert R. Flavell, Department of Radiology and Biomedical Imaging, University of California San Francisco, San Francisco, CA 94143. E-mail: robert.flavell@ucsf.edu

Mol Cancer Ther 2025;24:141–51

doi: 10.1158/1535-7163.MCT-24-0024

a StarPEG$_{40kDa}$ nanocarrier–based companion diagnostic for PEG-(SN-38)$_4$ and tested it in MX-1 (breast) and HT-29 (colorectal) tumor xenografts. The companion PET imaging surrogate with three SN-38 moieties and one deferoxamine B (DFB) demonstrated high accumulation in those tumor models and simultaneously identified the tumors suitable for PEG-(SN-38)$_4$ treatment (6). Furthermore, we evaluated the therapeutic efficacy of a nontargeted StarPEG$_{40kDa}$ nanocarrier with four copies of talazoparib (TLZ), PEG-TLZ$_4$, in breast and colon cancer xenografts (18), in which one single intraperitoneal (i.p.) dose of PEG-TLZ$_4$ was as potent as 30 daily oral doses of free TLZ in suppressing tumor growth. Thus, by monitoring the EPR-based passive uptake of a companion PET imaging surrogate, it may be possible to identify tumors that are most likely to benefit from nanocarrier-based therapies, thereby enabling personalized treatment options (6, 18–24). In this study, we developed a pair of companion PET imaging surrogates radiolabeled with ^{89}Zr, [^{89}Zr]PEG-DFB$_4$, and [^{89}Zr]PEG-DFB$_1$-TLZ$_3$, with or without the PARP inhibitor (PARPi) TLZ to predict heterogeneity in prostate cancer tumor models, which may help to predict the delivery and therapeutic efficacy of starPEG-TLZ$_4$ (25).

Materials and Methods

Materials and instrumentations

^{89}Zr oxalate was procured from 3D Imaging, p-SCN-Bn-deferoxamine from Macrocyclics, and deferoxamine mesylate from Sigma-Aldrich. The 4-armed PEG$_{40kDa}$-(NH$_2$)$_4$ was purchased from SINOPEG. TLZ was purchased from ApexBio or MedKoo. FBS, penicillin–streptomycin solutions, and RPMI 1640 media were purchased from Life Technologies, Thermo Fisher Scientific. Other chemicals (solvents, reagents, and building blocks) were purchased from Thermo Fisher Scientific, VWR, or Sigma-Aldrich and were used without further processing. Synthetic reactions were monitored using a high-performance liquid chromatography (HPLC) mobile phase of H$_2$O/0.1% trifluoroacetic acid and MeCN/0.1% trifluoroacetic acid. HPLC analyses were performed on either a Shimadzu LC-20AD HPLC system equipped with an SPD-M20A diode array detector and RF-10AXL fluorescence detector or an SPD-M20A diode array detector and an Alltech 3300 evaporative light scattering detector (ELSD), fitted with a Phenomenex Jupiter 5-μm C18 column (300 Å, 150 × 4.6 mm). Preparative HPLC was performed on a Shimadzu LC-20AP system equipped with a Phenomenex Jupiter C18 column (300 Å, 150 × 21.2 mm), FRC-10A fraction collector, and SPD-20A UV-vis detector. UV-vis data were acquired on a Hewlett Packard 8453 UV-vis spectrometer. Transmission electron microscopy images were recorded in a JEOL JEM-1230 instrument by loading the sample on a carbon-coated copper grid of 200 mesh. The surface charge (zeta potential) of the nanocarriers was obtained using a Malvern Zetasizer instrument.

Synthesis of starPEG conjugates

The synthetic procedures for the PET imaging surrogate of PEG-TLZ$_4$ and their respective nonreleasable TLZ linker and their conjugation to starPEG nanocarriers were derived from prior literature (6, 18).

Cell culture

Cells were obtained from the ATCC. Cell lines used in our studies were verified from the ATCC by short tandem repeat (STR) phenotyping and were tested negative for *Mycoplasma* contamination in bioluminescence-based MycoAlert Mycoplasma Detection Kit. The prostate cancer cell lines 22Rv1 (Cat# CRL-2505; RRID: CVCL_1045; passage number 06–14), DU145 (Cat# HTB-81; RRID: CVCL_0105; passage number 04–11), and PC3 (Cat# CRL-1435; RRID: CVCL_0035; passage number 08–15), pancreatic cancer cell line BxPC3 (RRID: CVCL_0186; passage number 04–09), and colon carcinoma cell line CT26 (Cat# CRL-2638; RRID: CVCL_7254; passage number 04–09) were cultured in RPMI 1640 medium containing 10% FBS and 1% penicillin/streptomycin at 37°C with 5% CO$_2$. According to experimental protocols, the cells were trypsinized (0.25%) for 2 to 3 minutes, and the cell suspensions were prepared in RPMI 1640 media for further passage or for s.c. tumor inoculation or in PBS for kidney and cardiac injections.

^{89}Zr radiolabeling of starPEGs

^{89}Zr-oxalate (7 μL, ~150 MBq) was neutralized with 7 μL of Na$_2$CO$_3$ (1 mol/L), and 500 μL of NH$_4$OAc (1 mol/L) was added to the mixture. To this mixture, ~3 mg of starPEG conjugates in 80 μL deionized DI water were added and incubated for 30 minutes at 25°C. The radiolabeled mixture was purified in a PD-10 size-exclusion desalting column (Thermo Fisher Scientific) and eluted with saline. Silica gel–impregnated glass microfiber chromatography paper (Neta Scientific) was used for instant thin-layer chromatography using 50 mmol/L ethylenediaminetetraacetic acid (EDTA) solution as mobile phase to confirm radiolabeling purity. The isolated bound activities were 131 to 146 MBq. The specific activity ranged from 43.6 to 48.6 MBq/mg.

S.c. and metastatic tumor models

A standard protocol approved by the University of California, San Francisco (UCSF) Institutional Animal Care & Use Committee has been followed for all the *in vivo* animal studies. All the mice used in our studies were male mice because prostate cancer is exclusively a disease of men. The animals were housed in a facility with a 12-hour light or day cycle with free access to food and water. For s.c. tumor models, the respective cells were suspended in 1:1 (v/v) Matrigel and serum-free media, and 4 to 5 weeks old homozygous (nu/nu; strain#: 002019) athymic male mice (Jackson Laboratories or Envigo-Harlan Laboratories) were inoculated with 22Rv1 (2.5 million), PC3 (2.5 million), DU145 (2.5 million), CT26 (1 million), and BxPC3 (2.5 million) cells in the left flank. Tumor size was 100 to 200 mm^3 after 1 to 2 weeks post-inoculation.

The patient-derived xenografts (PDX, LTL-545 and LTL-610) were obtained from Living Tumor Laboratory. For LTL-545 and LTL-610, 8 to 10 weeks old male NOD-SCID gamma (NOD.Cg-Prkdcscid Il2rgtm1Wjl/SzJ, strain#: 005557) mice were implanted subcutaneously in 50% Matrigel in the left flank with patient-derived tissue, as previously described (26, 27). After 1 to 2 weeks post-inoculation, tumors were approximately 150 to 300 mm^3 and used for subsequent studies.

The metastatic models were obtained by injecting 1 million of 22Rv1 luciferase reporter cells either in the left kidney capsule (in 30 μL PBS) or by intracardiac injection (in 100 μL PBS) into the left ventricle of the heart of 6 to 8 weeks old homozygous (nu/nu; strain#: 002019) athymic male mice. Briefly, luminescent cells were generated by transducing 22Rv1 parental cells (ATCC) with the pLV-luciferase-neomycin *Lentivirus* (derived from Addgene, plasmid # 21375 from Dr. Bryan Welm) and selecting with G418 for at least 5 days. *Lentivirus* was produced using calcium phosphate transfection of HEK293T/LentiX cells (Takara) and concentrated using the LentiX Concentrator (Takara) according to the manufacturer's protocol. Intracardiac injections were performed by the UCSF Preclinical Therapeutic Core. Tumor growth was monitored by bioluminescence imaging (BLI).

BLI

Tumor growth for the metastatic models was monitored by BLI 1 to 2 weeks after cell inoculation. Luciferin (100 μL of 50 mg/mL solution) was injected intraperitoneally in each mouse, and BLI (60-second exposure) was performed following 10 minutes of incubation in a Xenogen IVIS100 imaging system (Xenogen). Using an oval region of interest (ROI), the luciferase signal intensity was quantified as radiance (photons/seconds/cm^2/steradian) in Living Image 4.0 software.

In vivo PET imaging and biodistribution studies

When the s.c. tumor size reached 100 to 200 mm^3, 1 to 3 weeks post-inoculation, or after having reasonable BLI signal in the metastatic models (1–5 × 10^7 photons/seconds/cm^2/steradian), the respective ^{89}Zr-radiolabeled starPEG nanocarriers were injected via the tail vein (~7.4 MBq in 100 μL of saline per mouse). The study population included seven mice per group. Four mice from each group were scanned at 24, 48, 72, and 96 hours after radiopharmaceutical injection in a microPET/CT imaging system (Inveon, Siemens Medical Solutions). PET data were acquired for 20 minutes in list mode, and the manufacturer's 2D ordered subset expectation maximization algorithm was used to reconstruct the data and normalized to the injected activity to parameterize images to percentage injected dose (%ID/cc). The open-source AMIDE software (http://amide.sourceforge.net/) was used to process the imaged data. One nonimaged mouse was euthanized at 24, 48, and 72 hours, with the remaining four microPET/CT-imaged mice euthanized at 96 hours after injection of the ^{89}Zr-radiolabeled starPEG nanocarriers. Blood was collected by cardiac puncture, and major organs were harvested, weighed, and analyzed in an automated gamma counter (Hidex). The percent injected dose per gram of tissue (%ID/g) was determined by comparing with radioactive standards. The tumors and other major organs were retrieved for autoradiography and tissue staining. The ROI on the tumor and few major organs were drawn by 3D ellipsoid in AMIDE software.

Modeling of time–activity curves and accumulation parameters

Pharmacokinetic models were used to fit tumor tissue and blood data and simulate the mass–time profiles of nanocarriers distribution in tissues of interest following the previously reported method (6, 28). The simulation included specific compartments of the tumor and the heart as well as a generalized compartment for all other remaining tissues.

Autoradiography

After gamma counting (Hidex), the tumors were flash-frozen on dry ice after embedding in optimal cutting temperature compound. The frozen tumor tissues were sectioned at a thickness of 20 μm in a microtome and mounted on iQID (ionizing radiation quantum 264 imaging detector) charged-particle digital autoradiography imaging systems (QScint Imaging Solutions, LLC), and acquisition was carried out for 15 hours at 2V. The raw autoradiography data were processed using ImageJ software.

IHC

Following organ biodistribution, the tissue sections of 10 μm thickness were collected on glass slides from optimal cutting temperature–embedded frozen organ samples. Routine histologic analysis was performed to study microscopic features of the tumor samples. Cryosections air-dried for 5 minutes were fixed with 4% paraformaldehyde for 10 minutes and stained with hematoxylin (VWR, Cat# 95057844) for 5 minutes. After 30 seconds of exposure to 1% acid alcohol (solution of 1 mL of 37% hydrochloric acid diluted with 99 mL of 70% ethanol) and treated with bluing reagent (VWR, Cat# 95057852) for 20 seconds, the sections were counterstained with eosin (VWR, Cat# 95057848) for 15 seconds. The stained tissue sections were mounted with Vecta Mount (Vector, Cat# H-5000) and scanned using Aperio AT2 (Leica; magnification 1:200) for analysis. Quantification was performed using Aperio Image Scope v.11.2.0.780.

Immunofluorescence

For CD31 immunostaining, cryosections of the s.c. tumors were air-dried at room temperature for 5 minutes and fixed in 1:1 methanol and acetone solution for 10 minutes at −20°C. The sections were treated with UltraCruz Blocking Reagent (ChemCruz, Cat# sc-516214) and incubated overnight with anti-CD31 (1:100, Abcam, Cat# AB222783). Alexa 647–conjugated secondary antibody (1:200, Cell Signaling Technology, Cat# 4414S) and nuclear stain 4',6-diamidino-2-phenylindole (DAPI; 2 μg/mL, Sigma-Aldrich, Cat# MBD0015) were used for signal detection. Images were obtained using a Zeiss microscope and analyzed with either FIJI (ImageJ) or ZEN imaging software (Zeiss).

Statistical analysis

All data are presented as the mean ± SD in plots. The data were subjected to the Student *t* test (unpaired, two-tailed, and equal variance) for statistical analysis. Differences were considered significant at $P < 0.05$.

Data availability

The data presented in the current study are available within the article and the Supplementary Data or from the corresponding author on reasonable request.

Results

Design, synthesis, and radiolabeling of starPEG conjugates

Design of starPEG conjugates

The 40 kDa molecular weight and 15 nm size starPEGs provide an optimal size for longer blood circulation and EPR-mediated passive tumor accumulation depending on the tumor vasculature and macrophages (**Fig. 1A**; refs. 6, 12, 29). The primary goal of this study is to design a pair of companion imaging surrogates for a 4-armed starPEG$_{40kDa}$–based therapeutic nanodrug, PEG-TLZ$_4$, bearing four copies of releasable PARPi TLZ, and to evaluate if they can measure tumor heterogeneity and drug delivery in different cancer xenografts. In this study, we have designed and tested two starPEG nanodrugs without or with three copies of PARPi TLZ, which were conjugated to ^{89}Zr radiometal chelator DFB for PET imaging (**Fig. 1B**). A FDA-approved PEG polymer (30–32) was used as the backbone for the nanodrug and respective imaging surrogate.

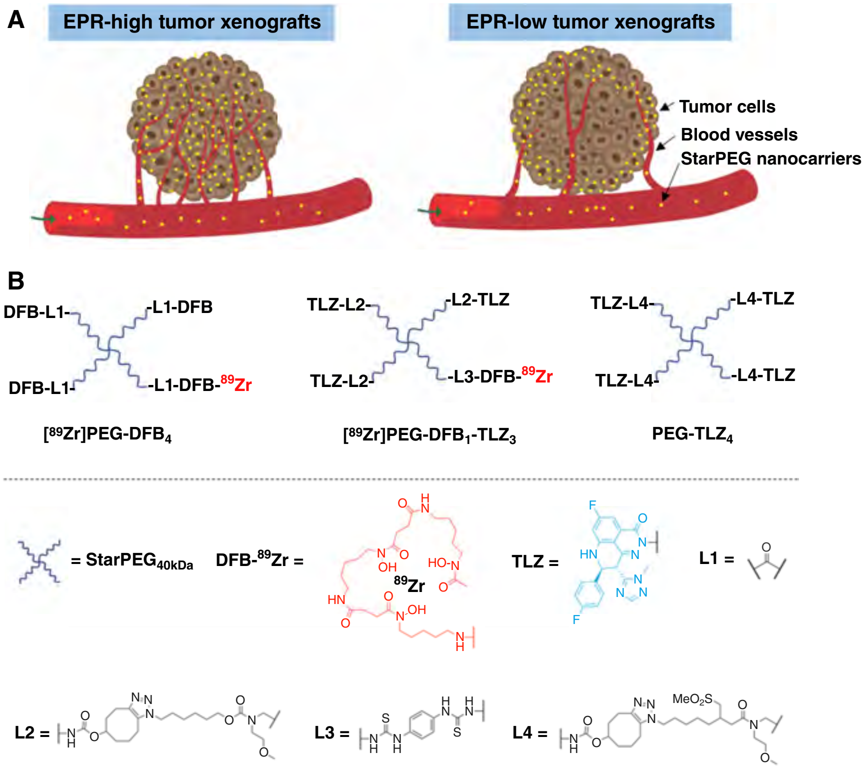

Figure 1.

EPR effect and design strategy of nanocarriers. **A,** Schematic presentation of StarPEG nanocarriers' accumulation and distribution in tumors with high vs. low vascularity. **B,** Schematic chemical structures of ^{89}Zr-labeled Star-PEG nanocarriers. Both the diagnostic nanocarriers, [^{89}Zr]PEG-(DFB)$_4$ and [^{89}Zr]PEG-(DFB)$_1$(TLZ)$_3$, were evaluated herein as companion PET imaging surrogates of the therapeutic nanocarrier PEG-TLZ$_4$.

Synthesis, characterization, and radiolabeling of starPEG conjugates

Both the companion PET imaging surrogates, PEG-DFB$_4$ and PEG-DFB$_1$-TLZ$_3$, were synthesized following previously reported synthetic routes (6, 33). Briefly, PEG-DFB$_4$ was synthesized by the reaction of the 4-armed PEG succinimidyl carbonate with deferoxamine mesylate. PEG-(5HCyO)$_3$(NH$_2$)$_1$ was used as the starting material to synthesize PEG-DFB$_1$-TLZ$_3$ using second-generation azide click reactions with cyclooctyne (6, 34). The azide counterpart Azido-TLZ was synthesized following a reported procedure as well (6, 18, 35, 36). PEG-(5HCyO)$_3$(NH$_2$)$_1$ conjugate with free amine was treated with isothiocyanatobenzyl-DFB to form PEG-(DFB)$_1$(5HCyO)$_3$ and was subsequently treated with Azido-TLZ to produce PEG-(DFB)$_1$(TLZ)$_3$. Overall, PEG-TLZ$_4$ is the therapeutic drug with releasable TLZ ligands, whereas two conjugates have been evaluated as companion PET imaging surrogates of PEG-TLZ$_4$, in which [^{89}Zr]PEG-(DFB)$_1$(TLZ)$_3$ bears three TLZ units via stable linkers. The nanocarriers were subjected to zetapotential measurement, demonstrating a near-neutral surface charge of -4.04 ± 0.21 and -1.41 ± 0.22 mV for PEG-DFB$_4$ and PEG-DFB$_1$-TLZ$_3$, respectively (Supplementary Fig. S1A). The sizes of the nanocarriers were evaluated by transmission electron microscopy analysis, which confirmed the particle size of approximately 10 to 15 nm (Supplementary Fig. S1B).

The radiolabeling of the respective starPEG conjugates with ^{89}Zr oxalate was performed in ammonium acetate buffer after neutralizing with sodium carbonate. The resulting complex was purified in a PD-10 size-exclusion desalting column by eluting with saline solution (33). The radiolabeling yield was 95% to 98% by instant thin-layer chromatography analysis, with isolated yields of 93% to 97% for PEG-(DFB)$_4$ ($n = 6$) and 87% to 95% ($n = 8$) for PEG-(DFB)$_1$(TLZ)$_3$. The specific activities ranged from 43.6 to 47.3 MBq/mg for PEG-(DFB)$_4$ and 46.3 to 48.6 MBq/mg for PEG-(DFB)$_1$(TLZ)$_3$.

In vivo microPET/CT imaging of s.c. tumor models

As a pilot study, one of the imaging surrogates, [^{89}Zr]PEG-(DFB)$_1$(TLZ)$_3$, was evaluated in five different tumor models, including the highly vascular CT26 (colorectal cancer), poorly vascular BxPC3 (pancreatic cancer), and a cross-section of prostate cancer tumor models (22Rv1, PC3, and DU145). As presented in Supplementary Figs. S2 and S3, the *in vivo* PET imaging, *ex vivo* biodistribution, and autoradiography studies demonstrated relatively higher and homogeneous tumor uptake in CT26 (15.1 ± 1.9 %IA/g), whereas moderate to low peripheral accumulation was observed in other tumor models (BxPC3: 8.4 ± 1.5 %IA/g; DU145: 6.9 ± 2.5 %IA/g; 22Rv1: 4.7 ± 0.8 %IA/g; and PC3: 4.2 ± 1.2 %IA/g; Supplementary Tables S1–S3). Our findings are in agreement with prior results (16), which demonstrated relatively low uptake in the prostate cancer models.

With these promising preliminary data in hand, we hypothesized that the designed PET imaging surrogates [^{89}Zr]PEG-(DFB)$_4$ and [^{89}Zr]PEG-(DFB)$_1$(TLZ)$_3$ may measure the magnitude and variability of the EPR effect in prostate cancer models. Different s.c. cell line–derived (22Rv1 and CT26) and patient-derived (PDXs LTL-545 and LTL-610) s.c. xenografts were tested for the EPR-mediated passive accumulation and distribution of the designed PET imaging surrogates, [^{89}Zr]PEG-(DFB)$_4$ and [^{89}Zr]PEG-(DFB)$_1$(TLZ)$_3$. As

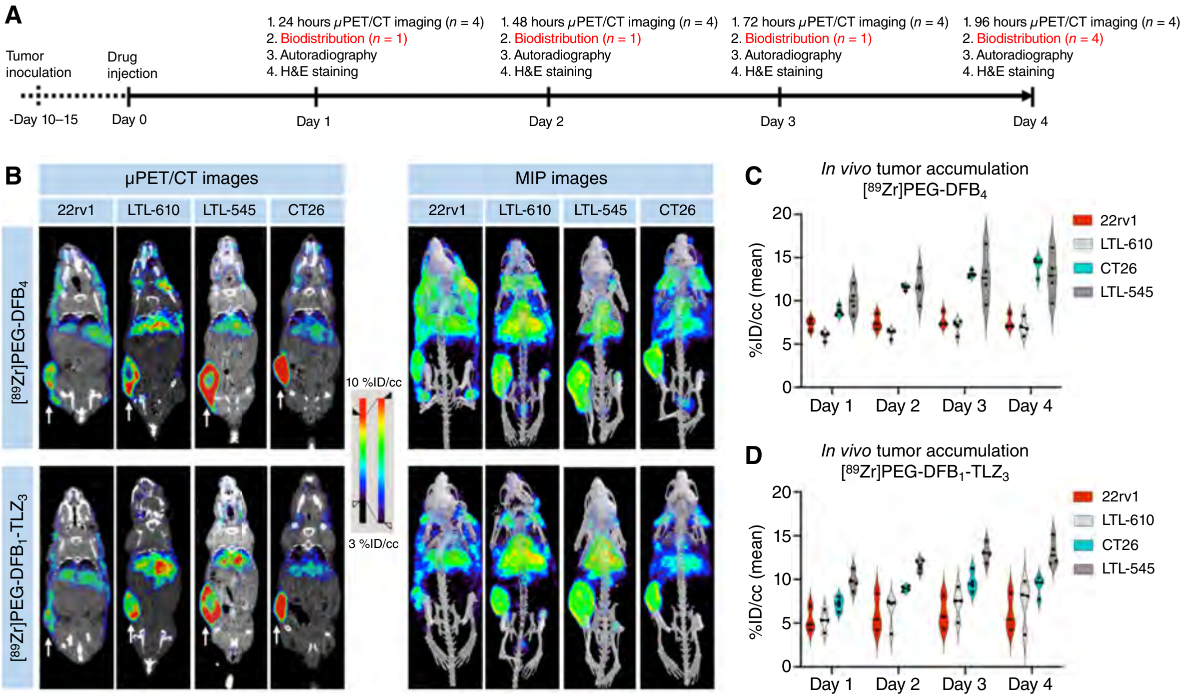

Figure 2.

In vivo microPET/CT imaging. **A,** Representation of the experimental design for *in vivo* evaluation of the ^{89}Zr-labeled starPEGs nanocarriers in mice bearing different s.c. xenografts over the left flank. **B,** Coronal microPET/CT and maximum-intensity projection microPET/CT obtained at 96 hours following the administration of ^{89}Zr-labeled starPEGs nanocarriers. Respective coronal microPET/CT and MIP images from days 1 to 4 are presented in Supplementary Materials (Supplementary Figs. S4–S7). **C** and **D,** Quantitative analysis of tumoral radiopharmaceutical accumulation based on ROI analysis on tumors from days 1 to 4 after the injection of ^{89}Zr-radiolabeled nanocarriers (n = 4, mean ± SD). MIP, maximum-intensity projection.

schematically presented in **Fig. 2A**, *in vivo* microPET/CT imaging of the ^{89}Zr-labeled nanocarriers over multiple time points was performed in the nu/nu athymic mice models bearing different s.c. tumors of around 150 to 300 mm^3 on the left flank.

The coronal microPET/CT and maximum-intensity projection images at 96 hours after injection of the nanocarriers are presented in **Fig. 2B**, and the respective serial images from days 1 to 4 are presented in Supplementary Figs. S4–S7. The microPET/CT images along with the respective ROI over tumors demonstrated relatively lower tumor uptake in 22Rv1 and LTL-610, whereas LTL-545 and CT26 showed higher tumor uptake. In the LTL-545 and CT26 models, the nanocarriers showed steady increase in tumor accumulation up to 72 hours and stabilized afterward. In contrast, they showed stable tumor accumulation starting from 24 hours in 22Rv1. ROI analysis demonstrated as high as 14.0 ± 1.0 %ID/cc accumulation of [^{89}Zr]PEG-(DFB)$_4$ in CT26 on day 4, whereas 12.9 ± 2.6, 7.5 ± 0.8, and 7.0 ± 1.0 %ID/cc accumulation were observed in LTL-545, 22Rv1, and LTL-610 xenografts, respectively (Supplementary Tables S4 and S5). However, [^{89}Zr]PEG-(DFB)$_1$(TLZ)$_3$ demonstrated the highest accumulation of 13.1 ± 1.5 %ID/cc in the LTL-545 xenograft compared with CT26 (9.2 ± 1.1 %ID/cc), LTL-610 (7.4 ± 2.6 %ID/cc), and 22Rv1 (6.0 ± 2.1 %ID/cc) tumors. Overall, the starPEG nanocarriers demonstrated variability in the EPR-mediated passive accumulation of the nanocarriers in different tumor models. The LTL-545 PDX model showed comparable passive tumor accumulation to that of known EPR-high CT26 colorectal tumor, whereas other prostate cancer models like 22Rv1 and LTL-610 had relatively low and heterogeneous tumor accumulation.

Ex vivo organ biodistribution

After serial PET imaging from days 1 to 4 after injection, the mice were sacrificed, and major organs and s.c. tumors were collected. The activity in the respective organs was counted in a gamma counter, and %ID/g tissue was calculated (Supplementary Figs. S8–S11; Supplementary Tables S6–S13). The *ex vivo* tumors' biodistribution of both the polymer nanocarriers on day 4 were compared, as shown in **Fig. 3**. [^{89}Zr]PEG-DFB$_4$ showed tumor accumulation of 6.56, 6.46, 13.19, and 17.98 %ID/g in 22Rv1, LTL-610, LTL-545, and CT26, respectively. [^{89}Zr]PEG-DFB$_1$-TLZ$_3$ showed tumor accumulation of 4.83, 9.07, 10.25, and 13.11 %ID/g in 22Rv1, LTL-610, LTL-545, and CT26, respectively. Except in CT26 tumor, both the nanocarriers demonstrated no significant variability among different s.c. tumor models (P values of 0.099, 0.078, 0.41 and 0.006 for 22Rv1, LTL-610, LTL-545, and CT26, respectively). The accumulation of [^{89}Zr]PEG-DFB$_4$ in both LTL-545 and CT26 are almost similar with no statistical significance *in vivo* ($P = 0.46$) and *ex vivo* ($P = 0.16$), but the accumulation of [^{89}Zr]PEG-DFB$_1$-TLZ$_3$ is statistically significant both *in vivo* ($P = 0.006$) and *ex vivo* ($P = 0.035$). Overall, comparatively higher uptake was seen in the CT26 and LTL-545 compared with 22Rv1 and LTL-610 xenografts. Besides, compared with [^{89}Zr]PEG-DFB$_4$, [^{89}Zr]PEG-DFB$_1$-TLZ$_3$

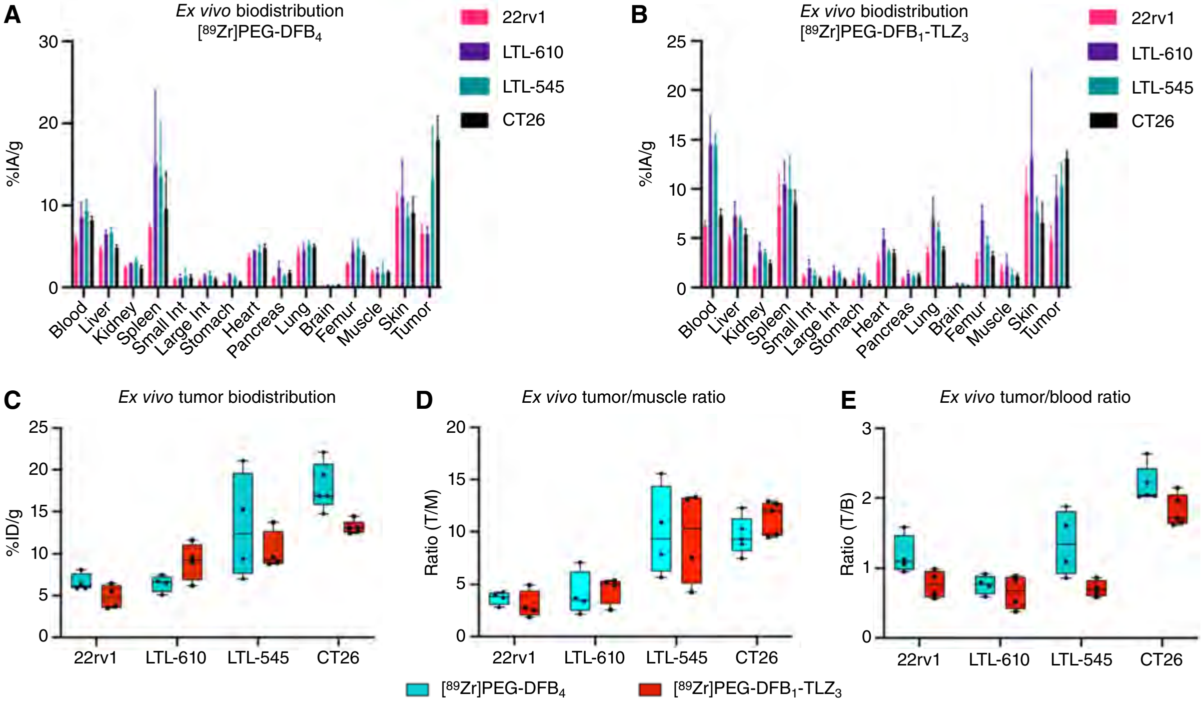

Figure 3.

Ex vivo organ biodistribution. *Ex vivo* organ biodistribution of (**A**) [^{89}Zr]PEG-DFB$_4$ and (**B**) [^{89}Zr]PEG-DFB$_1$-TLZ$_3$ nanocarriers in nude mice bearing different tumor xenografts at 96 hours after injection. Comparison of (**C**) *ex vivo* tumor biodistribution: (**D**) *ex vivo* tumor to muscle and (**E**) *ex vivo* tumor to blood ratios of the ^{89}Zr-labeled starPEG nanocarriers at 96 hours after injection ($n = 4$, mean ± SD). *Ex vivo* biodistribution of ^{89}Zr-labeled starPEG nanocarriers on selected major organs; the respective data tables are presented in Supplementary Materials (Supplementary Figs. S8–S11; Supplementary Tables S6–S13). Int, intestine.

showed relatively lower tumor accumulation and blood clearance (lower tumor/blood ratio; **Fig. 3C** and **E**).

Autoradiography and histology analyses

To explore the nanocarriers' tissue distribution, the s.c. tumors collected on days 1 to 4 after injection were dissected after gamma counting, and consecutive tissue sections were collected for autoradiography and histology analyses (**Fig. 4**; Supplementary Figs. S12–S15). Both nanocarriers with or without TLZ showed high and homogeneous deep-tumor penetration in the CT26 tumors. In contrast, the rest of the s.c. prostate cancer tumors like 22Rv1, LTL-545, and LTL-610 demonstrated only peripheral accumulation of the nanocarriers [^{89}Zr]PEG-DFB$_4$ and [^{89}Zr]PEG-DFB$_1$-TLZ$_3$. Such variation in the tumor distribution between CT26 and other prostate cancer tumor models could be due to the specific tumor vascularity and/or the presence of necrotic tissue in the tumor. Both the PDX models showed very high peripheral tumor accumulation, which could be in the soft tissue present on the tumor surface, as seen in LTL-610 tumors (Supplementary Fig. S16). For better understanding of the nature of passive accumulation and the influence of tumor vascularity, histology analysis was performed. As presented in Supplementary Figs. S12 and S13, hematoxylin and eosin staining of a few 22Rv1 and CT26 tumor sections from day 1 to 3 time points demonstrated large necrotic centers. Correlation of autoradiography and hematoxylin and eosin staining images demonstrated apparently paradoxical higher drug accumulation in the necrotic area in both 22Rv1 and CT26 tumors. However, despite healthy cancer cells, all the prostate cancer tumor models (LTL-545, LTL-610, and 22Rv1) demonstrated peripheral drug accumulation, whereas the colon cancer tumor model (CT26) showed homogeneous tissue penetrations. To further investigate the distinct tissue penetration between CT26 and other prostate cancer models, tumor vascularity was analyzed by immunofluorescent staining of CD31 present in the endothelial cell of both lymphatic and blood vessels with anti-CD31 antibody (Supplementary Fig. S17; refs. 37, 38). The CD31 staining results indicated homogenous vascular development in CT26, whereas the prostate cancer tumor models demonstrated heterogenous vasculature.

Pharmacokinetic analysis

Quantitative pharmacokinetics of influx (uptake) and release (efflux) of the StarPEG nanocarriers in tumors were determined from the sequential microPET/CT imaging up to 96 hours and shown in Supplementary Table S14. Data were fit according to previously reported procedures (6). The fraction of vascularized volume, which is basically the amount of blood in the organ, was estimated by extrapolation of the data to $t = 0$ and used to subtract signal from the tumor ROI due to blood. k_{in} and k_{out} are the first-order rate constants for uptake and release from the tissue after the blood components were subtracted, respectively. Although both the nanocarriers showed substantial tumor accumulation, the efflux

Figure 4.

Autoradiographic images and hematoxylin and eosin staining. Autoradiographic images and hematoxylin and eosin staining images of tumor sections collected after 96 hours after the injection of ^{89}Zr-labeled nanocarriers, demonstrating the variability of tumor accumulation and vasculature. Respective autoradiographic images and hematoxylin and eosin staining images from days 1 to 4 are presented in Supplementary Materials (Supplementary Figs. S12–S15). H&E, hematoxylin and eosin.

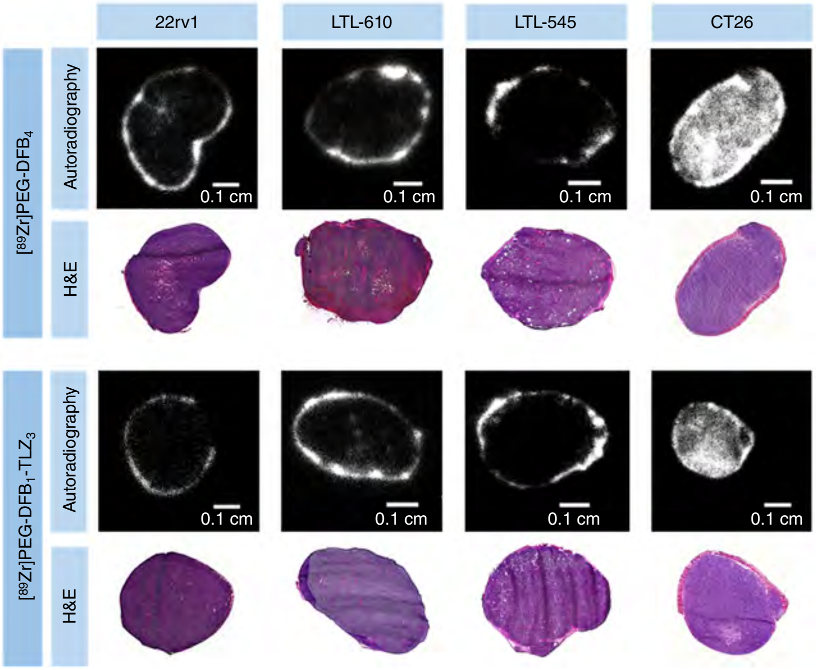

rates (k_{out}) may not be well-determined due to very long blood half-lives (typically >400 hours) of the nanocarriers as compared with the length of the current experiment (96 hours). In the case of [^{89}Zr]PEG-DFB$_4$ accumulation in CT26, the tumor accumulation was apparently still rising at the last data point (96 hours); in this case, the fit was constrained such that the tumor accumulation was considered maximal at the final data point. The resulting fits showed a good correlation between influx and efflux rates versus the mean %ID/g (**Fig. 5**). Although these correlations may be influenced by the relatively short duration of the accumulation experiments, it suggests that the studied xenografts all have similarly poor lymphatic development and associated low efflux rates and that tumor accumulation by both agents is primarily driven by the rate of influx.

Analysis of 22Rv1 spontaneous metastatic lesions

The EPR-mediated tumor accumulation of the nanocarrier was also tested in the 22Rv1 metastatic model by inoculating 22Rv1 cells stably expressing luciferase (22Rv1-Luc) directly into the kidney capsule. As shown in **Fig. 6A**, the mice were subjected to MRI that showed bright signal of axillary lymph node metastatic tumors. However, most of the mice grew multiple visible metastatic tumors at distinct locations like the thigh and neck regions, likely reflecting metastatic lymph nodes. For further confirmation of the 22Rv1 metastatic tumor, the mice were intraperitoneally injected with 100 µL of 50 mg/mL luciferin and were subjected to *in vivo* BLI before PET imaging (**Fig. 6B**; Supplementary Fig. S18). BLI of the mice demonstrated an intense bioluminescence signal at the metastatic axillary lymph node (white arrow). Serial PET imaging was

Figure 5.

Pharmacokinetic analysis. Correlation of influx and efflux rates with the mean %ID/g in the tumor as observed at the end of the experiment (96 hours). (For 22rv1, $n = 3$; for the rest, $n = 4$). k_{in}, *influx*; k_{out}, *efflux.*

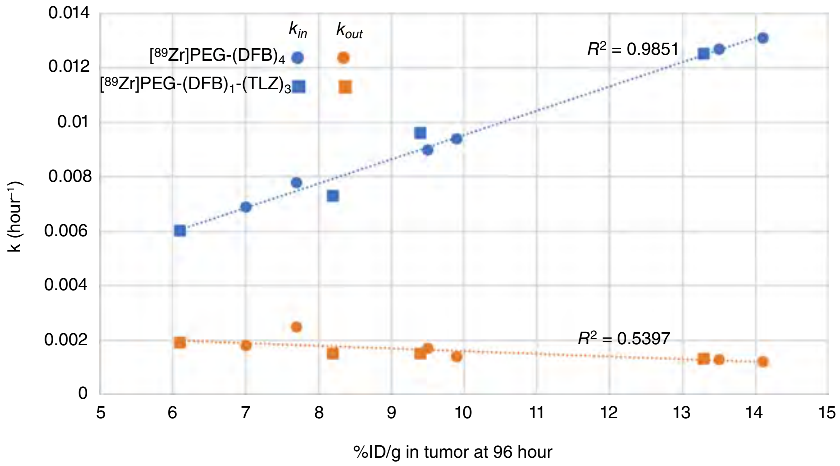

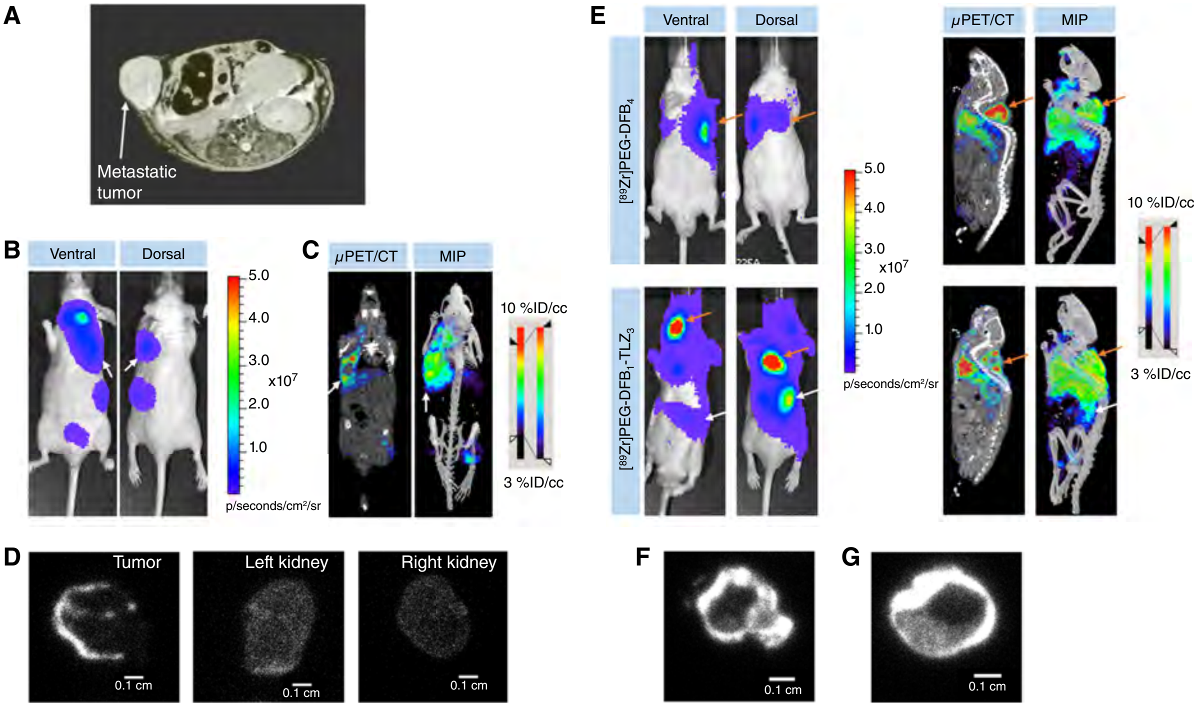

Figure 6.

Metastatic prostate cancer models demonstrate an EPR-low phenotype by PET imaging. **A,** *In vivo* MRI images before drug injection showing s.c. axillary lymph node metastatic tumors near the left arm. **B,** *In vivo* BLI nude mice inoculated with **22Rv1-Luc** cells in the left kidney capsule obtained before injection of the ^{89}Zr-labeled starPEG. White arrows indicate axillary node metastasis. **C,** Coronal microPET/CT and maximum-intensity projection microPET/CT obtained at 96 hours following the administration [^{89}Zr]PEG-DFB$_1$-TLZ$_3$ in nude mice inoculated with **22Rv1-Luc** cells in the left kidney capsule. White arrows indicate axillary node metastasis. Respective coronal microPET/CT and MIP images from days 1 to 4 are presented in Supplementary Materials (Supplementary Fig. S19). **D,** Autoradiographic images of the metastatic tumor and kidney sections collected after 96 hours after the injection of [^{89}Zr]PEG-DFB$_1$-TLZ$_3$. Respective autoradiographic images and hematoxylin and eosin staining images from days 1 to 4 are presented in Supplementary Materials (Supplementary Fig. S21). **E,** *In vivo* BLI, sagittal microPET/CT, and maximum-intensity projection microPET/CT obtained at 72 hours following the administration of the ^{89}Zr-labeled starPEG nanocarriers in nude mice via intracardiac inoculation of 22Rv1-Luc cells. Red arrows indicate metastasis on the back of the neck, and white arrows indicate liver metastasis. Autoradiographic images of the metastatic tumor were collected 72 hours after the injection of (**F**) [^{89}Zr]PEG-DFB$_4$ or (**G**) [^{89}Zr]PEG-DFB$_1$-TLZ$_3$ nanocarrier.MIP, maximum-intensity projection.

performed on the mice from days 1 to 4 after injection of [^{89}Zr]PEG-DFB$_1$-TLZ$_3$ (**Fig. 6C**; Supplementary Fig. S19). Noticable accumulation of the nanocarrier was observed in the metastatic axillary lymph node (white arrow) but was heterogenous in nature, similar to s.c. 22Rv1 xenografts. Organ biodistribution after 96 hours of drug injection demonstrated almost similar accumulation of the nanocarrier in both kidneys (left kidney: 2.46 %ID/g; right kidney: 2.58 %ID/g), whereas around 3.55 ± 1.06 %ID/g accumulation of the nanocarrier was observed in the metastatic solid tumors collected from the neck, axilla, or thigh region (Supplementary Fig. S20; Supplementary Tables S15 and S16). The kidneys and tumor tissues were dissected, and the tissue sections were subjected to autoradiography and histology analyses (Supplementary Figs. S6D and S21). Similar to the s.c. model, the metastatic solid tumors of 22Rv1 demonstrated heterogeneous peripheral accumulation of the nanocarrier.

In addition, the tumor accumulation and distribution of both the nanocarriers were also tested in disseminated 22Rv1-Luc metastatic models, prepared by intracardiac injection of the tumor cells. BLI signal indicated the presence of metastatic tumors on the back of the neck (red arrow) and in the liver (white arrow; **Fig. 6E**; Supplementary Fig. S22). Seventy-two hours after injection of the radiolabeled nanocarriers, *in vivo* microPET/CT imaging was performed, followed by *ex vivo* organ biodistribution and autoradiography. As presented in **Fig. 6E** and Supplementary Fig. S23, microPET/CT imaging and organ biodistribution demonstrated noticeable accumulation of both the nanocarriers in the metastatic tumors at the neck region, but they were heterogenous in nature, similar to s.c. 22Rv1 xenografts (Supplementary Tables S17 and S18). The metastatic tumors were dissected, and the tissue sections were subjected to autoradiography analysis (**Fig. 6F**). Similar to the s.c. model, the metastatic solid tumors of 22Rv1 demonstrated heterogeneous peripheral accumulation of the nanocarriers.

Discussion

The goal of this study was to design a pair of companion PET imaging surrogates for a 4-armed starPEG$_{40kDa}$ nanocarrier, PEG-TLZ$_4$, which possesses four copies of releasable PARPi TLZ, and to evaluate if the imaging surrogate can measure tumor heterogeneity in different cancer xenografts (**Fig. 1A**). In this study, we have designed two PET imaging surrogates of PEG-TLZ$_4$, i.e., PEG-DFB$_4$

and PEG-DFB$_1$-TLZ$_3$, by replacing either one or four TLZ units of the 4-armed starPEG$_{40kDa}$ (hydrodynamic diameter of 15 nm) with ^{89}Zr chelator DFB for PET imaging (**Fig. 1B**; ref. 39). Our prior study of nontargeted [^{89}Zr]PEG-DFB$_4$ nanocarrier in MX-1 (breast cancer) and HT-29 (colorectal cancer) tumor models demonstrated very high homogeneous passive accumulation and retention (>10 % ID 9 days after injection), which is an indicator of tumor models with high EPR status (6). In this study, the designed imaging surrogates were evaluated in various prostate cancer s.c. xenografts (22Rv1, LTL-545, and LTL-610) and metastatic models (22Rv1), and their tumor accumulation and distribution were compared with known EPR-high colorectal (CT26) and EPR-low pancreatic (BxPC3) tumor models (15).

The 4-armed StarPEG$_{40kDa}$ nanocarriers of around 15 nm size were strategically chosen to provide an optimal size for extended half-life and promote EPR-based tumor accumulation (6, 29). The multi-armed StarPEG could accommodate multiple copies of therapeutic as well as imaging scaffolds for better theranostic efficacy. Prior reports on 15 nm sized StarPEG$_{40kDa}$ nanocarriers conjugated with four copies of TLZ via stable linkers demonstrated very high treatment efficacy in tumor xenografts of breast and colon cancers (18). It was observed that one single i.p. dose of PEG-TLZ$_4$ was as potent as 30 daily oral doses of free TLZ in suppressing the tumor growth due to the long half-life and EPR-mediated optimum tumor accumulation of the nontargeted StarPEG nanocarrier. However, reports demonstrate that along with the nanocarrier size, EPR-directed pharmacokinetics of passive uptake is strongly influenced by tumor macrophages and vasculature (8, 12, 15, 16). For example, nontargeted polymer nanostars demonstrated very efficient tumor penetration and accumulation in CT26 tumors but were unable to penetrate deep into BxPC3 tumors, showing low peripheral tumor accumulation (15). Notably, most of the prostate cancer tumor models like CWR22Rv1, DU145, and PC3 have been shown to be of the EPR-low phenotype, with low overall tumor accumulation which is concentrated about the periphery (15–17). Thus, developing an imaging surrogate for the previously evaluated EPR-based potent StarPEG therapeutic scaffold, PEG-TLZ$_4$, emerges as a top priority (18). This surrogate has the potential to aid in the identification of patients with cancer with specific tumor types who are likely to benefit from the treatment (**Fig. 1**).

In this regard, two StarPEG nanocarriers, PEG-DFB$_4$ and PEG-DFB$_1$-TLZ$_3$, were synthesized as PET imaging surrogates and were radiolabeled with ^{89}Zr radiometal with good yields following the reported method (**Fig. 1B**; refs. 3, 6, 18). As a pilot study and to recapitulate the prior findings by Lewis and colleagues (15, 16), i.e., strong influence of the tumor vasculature in the EPR-mediated passive uptake and distribution, one of the imaging surrogate, [^{89}Zr] PEG-(DFB)$_1$(TLZ)$_3$, was evaluated in five different tumor models (CT26, BxPC3, 22Rv1, PC3, and DU145). Similar to the prior reports, at 72 hours after injection, relatively higher and homogeneous tumor accumulation was observed in CT26 with leaky vasculature, whereas moderate to low heterogeneous peripheral accumulation was observed in other tumor models with poor vasculature (Supplementary Figs. S2 and S3). Moreover, it was also observed that most of the prostate cancer models bear poor vasculature and undergo heterogeneous peripheral tumor accumulation (16). To gain more insight into the EPR-mediated passive accumulation, we further investigated the starPEG nanocarriers in other prostate cancer s.c., metastatic, and PDX models.

Both the nanocarriers were tested in four different s.c. tumor models, including three prostate cancers, in which serial microPET/CT imaging was performed from days 1 to 4 after injection, followed by organ biodistribution, autoradiography, and histology analysis on day 4 after imaging (**Fig. 2A**). Both nanocarriers showed very comparable *in vivo* and *ex vivo* accumulation in different xenografts, in which relatively higher accumulation of the nanocarriers was observed in both CT26 and LTL-545 and moderate to low accumulation was observed in LTL-610 and 22Rv1 (**Fig. 3**). In most of the tumor models, [^{89}Zr]PEG-DFB$_1$-TLZ$_3$ showed relatively lower blood clearance (lower tumor/blood ratio), which indicates relatively higher plasma interaction of TLZ to that of DFB. Tumor tissue was collected after gamma counting on days 1 to 4, which showed very efficient tumor penetration and homogenous distribution of the nanocarriers in CT26 tumors, whereas only peripheral tumor accumulation was observed in rest of the prostate cancer tumors (**Fig. 4**). It is interesting to note that despite improved *in vivo* and *ex vivo* accumulation in LTL-545 compared with LTL-610 and 22Rv1, both the nanocarriers demonstrated only peripheral accumulation and poor tissue penetration in LTL-545 tumor, which was observed in both coronal PET images and autoradiography images (**Figs. 2B** and **4**). The PDXs bear a relatively distinct peripheral soft tissue, resulting in higher peripheral accumulation to that of 22rv1, best seen on autoradiographic imaging (Supplementary Fig. S16). However, the overall tissue penetration of the nanocarriers was poor in these prostate cancer xenografts (22rv1 and PDXs) due to the relatively lower vascularity compared with that of CT26, as observed in CD31 staining (Supplementary Fig. S17). These observed results were in line with prior literature, in which prostate cancer tumor models demonstrated poor vascularity and underwent heterogeneous peripheral accumulation of the nontargeted nanocarriers (9, 15, 16). The histologic analysis of the tumor sections demonstrated large necrotic centers in some of the 22Rv1 and CT26 tumor sections (Supplementary Figs. S12 and S13). However, all the prostate cancer tumor models irrespective of necrotic centers undergo heterogeneous peripheral accumulation, whereas the colon cancer tumor model showed EPR-mediated homogenous distribution of both the nanocarriers (**Fig. 4**). Accordingly, CD31 staining of the tumor sections further confirmed homogenous vascular development in CT26, whereas heterogeneous vasculature was observed in all of the prostate cancer tumor models, which is in line with prior reports as well (15, 16, 37, 38).

Next, we evaluated the efficacy of the EPR-mediated imaging of the nanocarriers in metastatic tumor models. Metastatic tumor models of 22Rv1 cells were developed either by inoculating the cells directly into the kidney capsule or into the left ventricle of the heart by intracardiac injection. Luminescent 22Rv1 cell lines stably expressing luciferase were used for those studies, in which growth of metastatic tumors near the neck, axilla, or thigh region was observed by BLI after 7 to 8 weeks of cell inoculation (**Fig. 6B** and **E**). It was observed in the PET imaging that both the nontargeted StarPEG nanocarriers were efficiently accumulated in the metastatic tumors grown via cell inoculation in the kidney or in the heart (**Fig. 6C** and **E**). However similar to prostate cancer s.c. tumors, the PET and autoradiography images demonstrated heterogenous peripheral accumulation of the nanocarriers in 22Rv1 metastatic bulk tumors (**Fig. 6D** and **F**).

Overall, this result suggested that the nontargeted nanocarriers can efficiently measure the EPR effect in s.c. and metastatic bulk tumors. Both the nanocarriers demonstrated similar *in vivo* pharmacokinetics, which suggested that the designed PET imaging surrogate may predict patients with cancer with specific tumor types who are likely to benefit from the treatment of the therapeutic nanocarrier PEG-TLZ$_4$. The comparative analysis of these PET imaging surrogates could be promising in correlating the diagnostic and therapeutic delivery, which could be a potential future direction of this study along with clinical translation. The only major distinction between the imaging surrogates with different numbers of DFB or TLZ units is that the incorporation of TLZ units increases the plasma interaction in [^{89}Zr] PEG-DFB$_1$-TLZ$_3$ with relatively lower blood clearance to that of [^{89}Zr]PEG-DFB$_4$. Because the size and other physicochemical properties of the nanocarriers primarily control their *in vivo* pharmacokinetics and considering marginal influence of the conjugated imaging (DFB) and therapeutic (TLZ) ligands, those imaging surrogates could also be useful in screening patients with cancer with different tumor type likely to benefit from the treatment of other StarPEG therapeutic nanocarriers like PEG-(SN38)$_4$ (6). Our potential future direction is to quantitatively correlate the delivery of the PET imaging surrogates with their respective therapeutic nanocarriers along with their clinical translation.

Conclusion

In conclusion, our results indicate that the tumor uptake of the developed companion PET imaging surrogates, [^{89}Zr]PEG-DFB$_4$ and [^{89}Zr]PEG-DFB$_1$-TLZ$_3$, can measure the EPR effect in different cancer phenotypes. Our findings suggest that this approach has the potential to enable personalized treatment options and could screen the cancer type most likely to benefit from the PARPi-based PEG-TLZ$_4$ chemotherapeutic drug and other StarPEG nanocarriers as well. The potential for clinical translation of our approach could ultimately lead to improved treatment options and outcomes for patients with cancer.

Authors' Disclosures

N. Meher reports NA. S.D. Fontaine reports other support from ProLynx Inc. during the conduct of the study. R.R. Aggarwal reports grants from Amgen and Merck, personal fees from MJH Health, Flare Therapeutics, Novartis, Pfizer, Curio, Boxer Capital, and EcoR1, and grants and personal fees from Johnson and Johnson and AstraZeneca outside the submitted work. J. Chou reports grants from the NIH/NCI, the Prostate Cancer Foundation, the Bladder Cancer Advocacy Network, and DOD Prostate Cancer Research Program and personal fees from Exai Bio outside the submitted work. Y. Seo reports other support from Fortis Therapeutics, Inc. outside the submitted work. G.W. Ashley reports personal fees from ProLynx, Inc. during the conduct of the study; in addition, G.W. Ashley has a patent for WO2019/140271 pending. H.F. VanBrocklin reports grants from the NIH/NCI during the conduct of the study. R.R. Flavell reports grants from the NIH and the Department of Defense during the conduct of the study and grants and nonfinancial support from Fibrogen/Fortis and grants from Bristol Myers Squibb outside the submitted work; in addition, R.R. Flavell has a patent for PROSTATE-SPECIFIC MEMBRANE ANTIGEN–TARGETED DEEP-TUMOR PENETRATION OF POLYMER NANODRUGS AND METHODS OF USE THEREOF issued. No disclosures were reported by the other authors.

Authors' Contributions

N. Meher: Conceptualization, data curation, software, formal analysis, validation, investigation, visualization, methodology, writing–original draft, project administration, writing–review and editing. **A.P. Bidkar:** Data curation, software, formal analysis, validation, investigation, methodology, writing–review and editing. **A. Wadhwa:** Data curation, formal analysis, validation, writing–review and editing. **K.N. Bobba:** Data curation, formal analysis, validation, writing–review and editing. **S. Dhrona:** Data curation, software, formal analysis, writing–review and editing. **C. Dasari:** Data curation, software, formal analysis, validation, methodology, writing–review and editing. **C. Mu:** Data curation, methodology, writing–review and editing. **C.O.Y. Fong:** Data curation, software, writing–review and editing. **J.A. Cámara:** Data curation, methodology, writing–review and editing. **U. Ali:** Software, formal analysis, writing–review and editing. **M. Basak:** Data curation, software, visualization, methodology. **D. Bulkley:** Data curation, validation, visualization, methodology. **V. Steri:** Formal analysis, validation, writing–review and editing. **S.D. Fontaine:** Data curation, methodology, writing–review and editing. **J. Zhu:** Data curation, methodology, writing–review and editing. **A. Oskowitz:** Writing–review and editing. **R.R. Aggarwal:** Writing–review and editing. **R. Sriram:** Data curation, validation, methodology, writing–review and editing. **J. Chou:** Validation, methodology, writing–review and editing. **D.M. Wilson:** Writing–review and editing. **Y. Seo:** Validation, methodology, writing–review and editing. **D.V. Santi:** Validation, writing–review and editing. **G.W. Ashley:** Software, formal analysis, validation, methodology, writing–review and editing. **H.F. VanBrocklin:** Conceptualization, resources, formal analysis, supervision, funding acquisition, validation, investigation, visualization, methodology, project administration, writing–review and editing. **R.R. Flavell:** Conceptualization, resources, formal analysis, supervision, funding acquisition, validation, investigation, visualization, methodology, writing–original draft, project administration, writing–review and editing.

Acknowledgments

This project was funded by Cancer Center Support Grant P30CA082103, US Department of Defense Translational Science Award W81XWH-20-1-0292 (RRF), R01 CA266666, and the Cancer League (RRF), and the Precision Imaging of Cancer Therapy program (HFV). N. Meher thanks the Department of Science and Technology (DST), India, for the INSPIRE Faculty Fellowship.

Note

Supplementary data for this article are available at Molecular Cancer Therapeutics Online (http://mct.aacrjournals.org/).

Received January 15, 2024; revised April 5, 2024; accepted September 25, 2024; published first September 27, 2024.

References

1. Sung H, Ferlay J, Siegel R, Laversanne M, Soerjomataram I, Jemal A, et al. Global cancer statistics 2020: GLOBOCAN estimates of incidence and mortality worldwide for 36 cancers in 185 countries. CA Cancer J Clin 2021;71:209–49.
2. Schirrmacher V. From chemotherapy to biological therapy: a review of novel concepts to reduce the side effects of systemic cancer treatment (review). Int J Oncol 2019;54:407–19.
3. Meher N, Ashley GW, Bidkar AP, Dhrona S, Fong C, Fontaine SD, et al. Prostate-specific membrane antigen targeted deep tumor penetration of polymer nanocarriers. ACS Appl Mater Interfaces 2022;14:50569–82.
4. Shi J, Kantoff PW, Wooster R, Farokhzad OC. Cancer nanomedicine: progress, challenges and opportunities. Nat Rev Cancer 2017;17:20–37.
5. Liu W, Chen B, Zheng H, Xing Y, Chen G, Zhou P, et al. Advances of nanomedicine in radiotherapy. Pharmaceutics 2021;13:1757.
6. Beckford Vera DR, Fontaine S, VanBrocklin H, Hearn B, Reid R, Ashley G, et al. PET imaging of the EPR effect in tumor xenografts using small 15 nm diameter polyethylene glycols labeled with zirconium-89. Mol Cancer Ther 2020;19:673–9.
7. Maeda H, Wu J, Sawa T, Matsumura Y, Hori K. Tumor vascular permeability and the EPR effect in macromolecular therapeutics: a review. J Control Release 2000;65:271–84.
8. Kobayashi H, Watanabe R, Choyke P. Improving conventional enhanced permeability and retention (EPR) effects; what is the appropriate target? Theranostics 2014;4:81–9.
9. Maeda H. Toward a full understanding of the EPR effect in primary and metastatic tumors as well as issues related to its heterogeneity. Adv Drug Deliv Rev 2015;91:3–6.
10. Banerjee SR, Foss CA, Horhota A, Pullambhatla M, McDonnell K, Zale S, et al. ^{111}In- and IRDye800CW-labeled PLA–PEG nanoparticle for imaging prostate-specific membrane antigen-expressing tissues. Biomacromolecules 2017;18:201–9.
11. Meher N, VanBrocklin HF, Wilson DM, Flavell RR. PSMA-targeted nanotheranostics for imaging and radiotherapy of prostate cancer. Pharmaceuticals 2023;16:315.
12. Yang Q, Guo N, Zhou Y, Chen J, Wei Q, Han M. The role of tumor-associated macrophages (TAMs) in tumor progression and relevant advance in targeted therapy. Acta Pharm Sin B 2020;10:2156–70.

13. Fang J, Nakamura H, Maeda H. The EPR effect: unique features of tumor blood vessels for drug delivery, factors involved, and limitations and augmentation of the effect. Adv Drug Deliv Rev 2011;63:136–51.
14. Maeda H. The link between infection and cancer: tumor vasculature, free radicals, and drug delivery to tumors via the EPR effect. Cancer Sci 2013;104:779–89.
15. Goos J, Cho A, Carter L, Dilling T, Davydova M, Mandleywala K, et al. Delivery of polymeric nanostars for molecular imaging and endoradiotherapy through the enhanced permeability and retention (EPR) effect. Theranostics 2020;10:567–84.
16. Heneweer C, Holland J, Divilov V, Carlin S, Lewis J. Magnitude of enhanced permeability and retention effect in tumors with different phenotypes: ^{89}Zr-albumin as a model system. J Nucl Med 2011;52:625–33.
17. Lim J, Guan B, Nham K, Hao G, Sun X, Simanek E. Tumor uptake of triazine dendrimers decorated with four, sixteen, and sixty-four PSMA-targeted ligands: passive versus active tumor targeting. Biomolecules 2019;9:421.
18. Fontaine S, Ashley G, Houghton P, Kurmasheva R, Diolaiti M, Ashworth A, et al. A very long-acting PARP inhibitor suppresses cancer cell growth in DNA repair-deficient tumor models. Cancer Res 2021;81:1076–86.
19. Dasgupta A, Biancacci I, Kiessling F, Lammers T. Imaging-assisted anticancer nanotherapy. Theranostics 2020;10:956–67.
20. Ehlerding EB, Grodzinski P, Cai W, Liu CH. Big potential from small agents: nanoparticles for imaging-based companion diagnostics. ACS Nano 2018;12: 2106–21.
21. Miedema IHC, Zwezerijnen GJC, Huisman MC, Doeleman E, Mathijssen RHJ, Lammers T, et al. PET-CT imaging of polymeric nanoparticle tumor accumulation in patients. Adv Mater 2022;34:2201043.
22. Pérez-Medina C, Teunissen AJP, Kluza E, Mulder WJM, van der Meel R. Nuclear imaging approaches facilitating nanomedicine translation. Adv Drug Deliv Rev 2020;154-155:123–41.
23. Chakravarty R, Hong H, Cai W. Positron emission tomography image-guided drug delivery: current status and future perspectives. Mol Pharm 2014;11:3777–97.
24. Yoon J-K, Park B-N, Ryu E-K, An Y-S, Lee S-J. Current perspectives on 89Zr-PET imaging. Int J Mol Sci 2020;21:4309.
25. Stewart RA, Pilié PG, Yap TA. Development of PARP and immune-checkpoint inhibitor combinations. Cancer Res 2018;78:6717–25.
26. Lin D, Wyatt AW, Xue H, Wang Y, Dong X, Haegert A, et al. High fidelity patient-derived xenografts for accelerating prostate cancer discovery and drug development. Cancer Res 2014;74:1272–83.
27. Chou J, Egusa EA, Wang S, Badura ML, Lee F, Bidkar AP, et al. Immunotherapeutic targeting and PET imaging of DLL3 in small-cell neuroendocrine prostate cancer. Cancer Res 2023;83:301–15.
28. Chauhan V, Stylianopoulos T, Martin J, Popović Z, Chen O, Kamoun W, et al. Normalization of tumour blood vessels improves the delivery of nanomedicines in a size-dependent manner. Nat Nanotechnol 2012;7: 383–8.
29. Singh Y, Gao D, Gu Z, Li S, Stein S, Sinko P. Noninvasive detection of passively targeted poly(ethylene glycol) nanocarriers in tumors. Mol Pharm 2012;9:144–55.
30. Barenholz Y. Doxil®—the first FDA-approved nano-drug: lessons learned. J Control Release 2012;160:117–34.
31. Barenholz Y, Braddock M. Doxil (R) - the first FDA-approved nano-drug: from basics via CMC, cell culture and animal studies to clinical use. In: Nanomedicines: Design, delivery and detection. Royal Society of Chemistry; 2016. pp. 315–45.
32. Barenholz Y, Peer D. Doxil—the first FDA-approved nano drug: from and idea to product. In: Peer D., editor. Hand book of harnessing biomaterials in nanomedicine: Preparation, Toxicity, and Applications. 2012. p. 335–398. Publisher: Taylor and Francis Group, Imprint: Jenny Stanford Publishing 10.1201/9781003125259-16
33. Perk L, Vosjan M, Visser G, Budde M, Jurek P, Kiefer G, et al. p-Isothiocyanatobenzyl-desferrioxamine: a new bifunctional chelate for facile radiolabeling of monoclonal antibodies with zirconium-89 for immuno-PET imaging. Eur J Nucl Med Mol Imaging 2010;37:250–9.
34. Jewett J, Bertozzi C. Cu-free click cycloaddition reactions in chemical biology. Chem Soc Rev 2010;39:1272–9.
35. Wang M, McNitt C, Wang H, Ma X, Scarry S, Wu Z, et al. The efficiency of ^{18}F labelling of a prostate specific membrane antigen ligand via strain-promoted azide–alkyne reaction: reaction speed versus hydrophilicity. Chem Commun 2018;54:7810–13.
36. Wang S, Blaha C, Santos R, Huynh T, Hayes T, Beckford-Vera D, et al. Synthesis and initial biological evaluation of boron-containing prostate-specific membrane antigen ligands for treatment of prostate cancer using boron neutron capture therapy. Mol Pharm 2019;16:3831–41.
37. Lertkiatmongkol P, Liao D, Mei H, Hu Y, Newman PJ. Endothelial functions of platelet/endothelial cell adhesion molecule-1 (CD31). Curr Opin Hematol 2016;23:253–9.
38. Diana A, Wang LM, D'Costa Z, Azad A, Silva M A, Soonawalla Z, et al. Prognostic role and correlation of CA9, CD31, CD68 and CD20 with the desmoplastic stroma in pancreatic ductal adenocarcinoma. Oncotarget 2016;7: 72819–32.
39. Deri M, Zeglis B, Francesconi L, Lewis J. PET imaging with 89Zr: from radiochemistry to the clinic. Nucl Med Biol 2013;40:3–14.